PROCESS SAFETY
PROGRESS

ORIGINAL ARTICLE

Charge distribution in turbulent flow of charged liquid—Modeling and experimental validation

Aaron D. Ratschow [1,2] ⓘ | Sigrun Stein [1] | Hans-Jürgen Gross [1]

[1]Department for Process and Plant Safety, Bayer AG, Leverkusen, Germany

[2]Institute for Nano- and Microfluidics, TU Darmstadt, Alarich-Weiss-Straße 10, D-64287, Darmstadt, Germany

Correspondence
Aaron D. Ratschow, Institute for Nano- and Microfluidics, TU Darmstadt, Alarich- Weiss-Straβe 10, D-64287, Darmstadt, Germany.
Email: contact@aaronratschow.de

Abstract

Electric discharges due to the flow of charged organic liquids are a common ignition source for explosions in the chemical and process industry. Prevention of incidents requires knowledge of electric fields above the surface of charged liquids. Quantitative methods often estimate electric fields based on simplifying assumptions like homogeneous volumetric charge distribution and neglect of surface charge. More detailed electrohydrodynamic (EHD) models are only available for laminar flow regimes. This work presents a model for forced turbulent EHD flows of dielectric liquids based on Reynolds-averaged Navier–Stokes equations that predicts the electric field in the gas phase in good agreement with our experiments. We observe diminishing surface charge accumulation at the liquid surface with increasing flow velocities and thereby unify seemingly contradictory previous findings regarding the relevance of surface charge. The model can efficiently be applied to various industrial flow configurations and provide a central tool in preventing electrostatic hazards.

KEYWORDS
fire and explosion analysis, hazards evaluation, risk assessment

1 | INTRODUCTION

In many practical applications in the chemical and process industry organic liquids with low conductivity develop an electric charge. Electrostatic charging can occur in pipe flow or stirring in reactors or storage tanks, among other processes.[1,2] Accumulated charge leads to strong electric fields in the gas phase above the liquid surface and eventually to electric discharge. When an explosive atmosphere is present, electric discharges can act as ignition sources for explosions. Electrostatic incidents occur repeatedly in the industry.[3–6]

Despite growing theoretical knowledge of the underlying electrostatic phenomena, preventive and protective measures often rely on experience and empirical knowledge of experts.[7] Quantitative methods involving numerical simulations usually hinge on simplifying assumptions like homogeneous volume charge densities and neglect of surface

charge.[8–10] Detailed computations of volume charge distributions are only established in the investigation of small scale electrohydrodynamic (EHD) flow phenomena.[11–14] These models only apply to the laminar flow regime or direct numerical simulations of turbulent flows. Strongly coupled equations of fluid flow and electrostatics make them computationally expensive and thus unsuitable for assessment of industrial scale applications.

Furthermore, previous literature findings are ambiguous regarding the relevance of surface charge in EHD modeling. Several authors have published theoretical models of EHD flows or charge relaxation problems with free surfaces not accounting for surface charge.[8,11,15] This approach has led to good agreement with experimental data for the turbulent filling of large tanks with liquid volumes $V = \mathcal{O}(1\mathrm{m}^3)$[9,10,16] while surface charge accumulation was found to be significant in smaller scale experiments $V = \mathcal{O}(1 \times 10^{-8}\mathrm{m}^3)$[12] with negligible fluid

FIGURE 1   Schematics of the experimental setup (A) including the mounting rig for the electric field meter and position of the field meter in the rig (B).
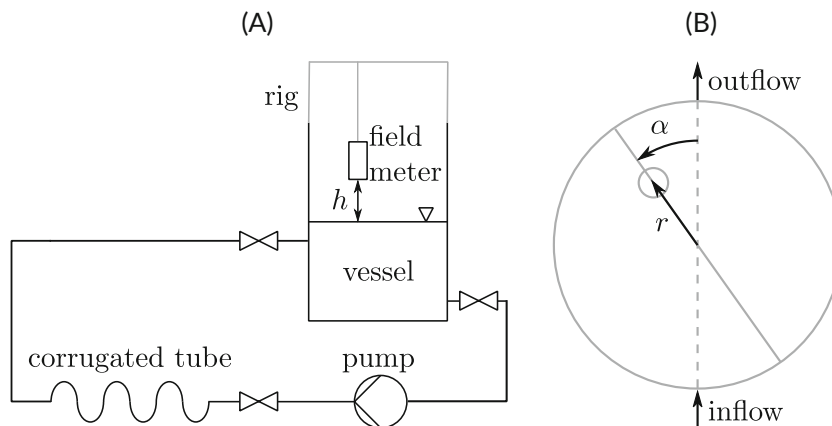
velocities or after pumping stopped in experiments with intermediate size vessels $V = \mathcal{O}(0.1\text{m}^3)$.[17] In addition to surface charge accumulation, surface conduction at gas–liquid interfaces has been discussed as a relevant transport mechanism.[17,18]

In this paper, we present a model with reduced mathematical coupling for calculating inhomogeneous volume charge distributions in turbulent flows under consideration of surface charge to predict electric fields above the liquid surface by combining modeling approaches for charge transport with Reynolds-averaged Navier–Stokes (RANS) equations. They are the industrial standard for modeling turbulent flow problems and, in contrast to direct numerical simulations, allow for efficient simulations of turbulent flows on large and complex geometries.[19] To validate the model, we present experiments of a charged jet entering a partially filled vessel below the surface (see Figure 1) and showcase essential implications regarding the influence of surface charge accumulation. This method is a step toward quantitative prediction of electrostatic hazards in the chemical and process industry for improved explosion prevention.

2 | MATHEMATICAL MODELING AND COMPUTATIONS

In this section, we motivate and justify means of reducing the mathematical coupling of the governing equations for EHD flows including surface charge. We then give boundary conditions as well as details on the numerical procedure.

2.1 | Governing equations with reduced coupling

The general set of governing equations for EHD flows of incompressible fluids are the Poisson-Nernst-Planck (PNP) and Navier–Stokes (NS) equations.[20] For low conductivity organic liquids, the local conductivity can be considered constant and the NP equations simplify to a single equation for space charge conservation, yielding

$$\frac{\partial \mathbf{u}}{\partial t} + (\mathbf{u} \cdot \nabla)\mathbf{u} = -\frac{1}{\rho}\nabla p + \nu \nabla^2 \mathbf{u} + \frac{1}{\rho}\mathbf{f}_{el}, \nabla \cdot \mathbf{u} = 0, \quad (1a)$$

$$\nabla \cdot \mathbf{E} = \frac{\rho_v}{\epsilon}, \mathbf{E} = -\nabla\Phi, \quad (1b)$$

$$\frac{\partial \rho_v}{\partial t} + \nabla \cdot \mathbf{J} = 0, \quad (1c)$$

where $\mathbf{u}$ is the velocity, ρ is the fluid density, p is the pressure, ν is the kinematic viscosity, $\mathbf{E}$ is the electric field, ρ_v is the volumetric free charge density, ϵ is the electric permittivity, and Φ is the electric potential.[21] The current density vector $\mathbf{J}$ is then given by

$$\mathbf{J} = \rho_v \mathbf{u} - D\nabla^2\rho_v + \kappa\mathbf{E}, \quad (2)$$

where κ is the electric conductivity and D the effective charge diffusivity. Equations (1a)–(1c) are generally strongly coupled through the electric volume force or Lorentz force

$$\mathbf{f}_{el} = \rho_v\mathbf{E} - \frac{1}{2}E^2\nabla\epsilon. \quad (3)$$

While this set of equations is very general and applicable to laminar flow problems as well as direct numerical simulation of turbulent flows, the strong mathematical coupling and non-linearity make it unsuitable for modeling industrial scale turbulent flow situations. To overcome this, we introduce and justify a number of simplifications.

Turbulent flow is generally characterized by a high Reynolds number

$$Re = \frac{\widetilde{U}\widetilde{L}_{fl}}{\nu}, \quad (4)$$

with the characteristic velocity $\widetilde{U}$ and length scales $\widetilde{L}_{fl}$, that expresses the ratio of inertial forces to viscous forces. Similarly, we propose a measure for the ratio of inertial forces and Lorentz forces to further characterize forced EHD flows. To this end, we introduce characteristic scales for different variables which are marked with $\widetilde{\cdot}$. For homogeneous fluids, ϵ is constant and thus Lorentz force simplifies to $\mathbf{f}_{el} = \rho_v\mathbf{E}$. With Gauss' law the electric field can be estimated,

$$\nabla \cdot \mathbf{E} = \frac{\rho_v}{\epsilon}, \frac{\widetilde{E}}{\widetilde{L}_{el}} \sim \frac{\widetilde{\rho}_v}{\epsilon}, \tag{5}$$

where $\widetilde{L}_{el}$ is a characteristic length scale of the electrostatic problem. The magnitude of the Lorentz forces $|\mathbf{f}_{el}| = f_{el}$ becomes

$$f_{el} \sim \frac{\widetilde{\rho}_v^2 \widetilde{L}_{el}}{\epsilon}, \tag{6}$$

and together with the magnitude of the inertial forces $|\mathbf{f}_{inertial}| = f_{inertial}$

$$f_{inertial} = |\rho(\mathbf{u} \cdot \nabla)\mathbf{u}| \sim \frac{\widetilde{\rho}\widetilde{U}^2}{\widetilde{L}_{fl}}, \tag{7}$$

the ratio becomes

$$\frac{f_{inertial}}{f_{el}} \sim \frac{\rho \epsilon \widetilde{U}^2}{\widetilde{\rho}_v^2 \widetilde{L}_{el} \widetilde{L}_{fl}} \equiv \Pi_{el}. \tag{8}$$

With similar length scales, $\widetilde{L}_{el} = \widetilde{L}_{inertial} = \widetilde{L}$, this ratio simplifies to

$$\Pi_{el} = \frac{\rho \epsilon \widetilde{U}^2}{\widetilde{\rho}_v^2 \widetilde{L}^2}. \tag{9}$$

If $\Pi_{el} \approx 1$ or even $\ll 1$, the flow is governed by electric forces. On the other hand, when $\Pi_{el} \gg 1$ their effect is small. When a turbulent flow with $Re \gg 1$ and $\Pi_{el} > Re$ is considered, Lorentz forces are negligible and the flow field is governed by inertial forces, effectively decoupling the flow field from the charge transport. These conditions apply to many technical flow configurations in the chemical and process industry like the one discussed in this paper. Consequently, the flow field can be computed independently in a first step, using RANS equations for industrial scale turbulence.

In turbulent flow, the effective diffusivity $D = D_\nu + D_T$ includes the molecular diffusivity D_ν and the turbulent mixing coefficient D_T. For dielectric fluids molecular diffusion is only relevant on the microscale and can be neglected on larger length scales.[12] Therefore effective diffusivity can be replaced with the turbulent mixing coefficient. Closing the electromigration term in Equation (2) with (1b) then leads to the simplified charge transport equation

$$\frac{\partial \rho_v}{\partial t} + \nabla \cdot (\rho_v \mathbf{u}) = D_T \nabla^2 \rho_v - \frac{\kappa}{\epsilon}\rho_v, \tag{10}$$

where the last term on the right-hand side describes Ohmic charge relaxation with the charge relaxation time $\tau_{rel} = \epsilon/\kappa$. Note that Equation (10) is mathematically coupled to the NS but not to the electrostatic Poisson equation. While turbulent mixing has previously been considered in models of flow electrification in turbulent pipe flows, the mixing coefficient has been modeled either as a constant in the bulk flow[22,23] or as a function of wall distance.[1] For more general or complex geometries we propose to model the turbulent mixing coefficient D_T, in analogy to turbulent heat and mass transfer, to be proportional to turbulent eddy viscosity ν_T:

$$D_T = \frac{\nu_T}{Sc_T}, \tag{11}$$

where Sc_T is the turbulent Schmidt number. Extensive research has been conducted on the turbulent Schmidt (or Prandtl) number in mass (or heat) transfer.[24–26] It is usually between 0.5 and 0.9, and varies with flow geometry but not between heat and mass transfer. In this work for an injection jet into a vessel Sc_T was specified as 0.7.[24]

During charge relaxation in the bulk liquid, charge is conducted along the electric field. At grounded conducting walls, like present in most industrial cases, the charge is neutralized by an opposite charge in the conducting wall. At non-conductive interfaces, like the liquid surface or enameled walls, surface ions form an effective surface charge.[21] We use the general form of an interfacial balance law reported by Kallendorf et al.[27] to derive a balance equation for surface charge density σ_s that is applicable to fluid/fluid and fluid/solid interfaces and reads

$$\frac{\partial \sigma_s}{\partial t} + \nabla_s \cdot (\sigma_s \mathbf{u}) = -\nabla_s \cdot (\lambda_s \mathbf{E}) + (\nabla_s \cdot \mathbf{n})(\lambda_s \mathbf{E} \cdot \mathbf{n}) + \mathbf{n} \cdot [\![\kappa \mathbf{E}]\!]. \tag{12}$$

The symbol $\nabla_s = \nabla - \mathbf{n} \cdot (\mathbf{n} \cdot \nabla)$ is the surface divergence operator and the second term on the left hand side describes advection along the surface. The first and second terms on the right hand side account for surface conduction with surface conductivity λ_s, as proposed and measured by Matsubara and Jones,[17,18] and total surface curvature $\nabla_s \cdot \mathbf{n}$. The last term on the right hand side is a charge conservative source term due to bulk conduction toward the surface. The symbol $[\![\Theta]\!]$ denotes a jump of Θ across the surface. In the present work, Equation (12) is solved on the liquid surface. The electric field is not continuous across a charged interface. Surface charge is therefore coupled to the Poisson equation by the interfacial condition $\mathbf{n} \cdot [\![\epsilon \mathbf{E}]\!] = \sigma_s$.

Equations (1b), (10), and (12) constitute a model for forced turbulent EHD flows of low-conducting liquids with reduced mathematical coupling. It can be applied to any RANS turbulence model without the need for a Lorentz force term if $\Pi_{el} > Re$. In this work, the turbulent jet into a vessel is modeled using the standard two-equation $k - \epsilon$−model. A more elaborate formulation of the model applicable to significantly deformed free surface flows and two-phase flows is given in Appendix A.

2.2 | Boundary conditions

The simulations performed in this work focus on a partially filled, flowed through vessel. The computational domains cover the gas phase inside the vessel, including a field meter or needle where

applicable, as well as the liquid phase inside the vessel (compare Figure 1). Inlet and outlet of the vessel are discretized as pipe sockets with a length to diameter ratio of 5 and the RANS equations are only solved in the liquid phase. All walls are treated as non-slip.

For the free surface, viscous stresses from the air are neglected because the dynamic viscosity and density of air are small compared to the liquid. The dimensionless Eötvös number $Eo = \rho g \widetilde{L}^2 / \gamma$, with the vessel diameter as a characteristic length scale $\widetilde{L}$, can be used to estimate the relative importance of surface tension γ at the free surface. Because of $Eo > 5 \times 10^5$ surface tension effects are neglected. Effects of the dynamic pressure on the free surface are assessed with the dimensionless Froude number $Fr = U / \sqrt{g\widetilde{L}}$ where U is the local velocity and the length scale $\widetilde{L}$ is the liquid level. Even when evaluated with the average inflow velocity, which is higher than local velocities near the free surface, $Fr < 1$ indicates only minimal deformations of the free surface, which also corresponds with experimental observations. A full computation of the deformed free surface with the model given in Appendix A shows the maximum surface deformation to be < 2.5 mm. Given the above, free surface deformation is deemed insignificant and the free surface is modeled as a fixed boundary with zero tangential stress.

At the inlet, a fully developed pipe flow profile is predefined using a dedicated feature within Comsol Multiphysics (for details the reader is referred to[28]). The volumetric charge density conservation Equation (10) requires a Dirichlet BC, $\rho_v = \rho_{v,in}$, at the inlet. At all remaining boundaries homogeneous Neumann BCs are assigned to suppress diffusive flux into the walls. The balance of surface charge, Equation (12), is solved on the liquid surface with Dirichlet BCs, $\sigma_s = 0$, on the edges where the surface meets grounded walls. All grounded metal parts are assigned the Dirichlet BC $\Phi = 0$ for the Poisson Equation (1b).

2.3 | Numerical procedure

All numerical calculations are performed using the commercial finite element code Comsol Multiphysics version 5.5.[29] The presented model consists of Equations (1b), (10), (12), and RANS equations with the standard two-equation $k - \epsilon$-model with parameters reported by Wilcox[30] and wall functions according to Cebeci.[31] Compared with the laminar model (Equations 1), coupling is significantly reduced through the neglect of Lorentz force due to $\Pi_{el} > Re \gg 1$. This makes the fluid flow approximately independent of electrostatics and allows for sequential solving of the model. The RANS equations are solved in the liquid domain in a first step. Subsequently, the transport of volume charge, Equation (10), is solved in the liquid domain, as it does not depend on the electric field explicitly. In a last step, the coupled Equations (12) and (1b) for surface charge and electric potential are solved simultaneously on the entire geometry including liquid and gas domains. This numerical procedure allows the fluid flow and volumetric charge equations to be solved on a numerical mesh optimized for fluid flow. The results are then mapped onto a mesh optimized for the electrostatic problem on which the surface charge and Poisson equations are solved.

Both meshes used throughout this work are consecutively refined using Comsol's adaptive mesh refinement feature[32] and mesh independence of the results is ensured. Velocity and pressure are discretized with linear and electric potential with cubic shape functions while all other variables use quadratic shape functions.

3 | EXPERIMENTAL PROCEDURE

For validation of the presented reduced model, experiments were conducted that focused on measuring the electric field above the liquid surface in different positions in a representative problem. This enabled the investigation of local charge transport and surface charge accumulation. In the following, we explain the experimental setup and the numerical method for determining the influence of the measurement equipment on the measured values.

3.1 | Experimental setup

In the experiments conducted for this work a charged liquid jet was injected into a vessel and the electric field above the liquid surface was measured. Liquid was circulated to provide quasi-stationary conditions. The experimental setup used is shown in Figure 1. It consisted of a cylindrical stainless steel vessel with an inner diameter of 480 mm and a height of 577 mm, a Calio 25–100 centrifugal pump by KSB and a 3 m stainless steel DN50 corrugated tube. The inflow and outflow of the vessel were 30 mm in diameter and located on opposite sides at heights 200 and 40 mm above the lower edge. All fluidic components were connected with silicone tubes and threads were sealed with PTFE tape. For measuring electric fields in the gas phase, a Fetronic FM-206 field meter with a cylindrical sensor was used. It was attached to the vessel with a rig that allowed for reproducible positioning of the field meter sensor above the liquid surface, as shown in Figure 1. A temperature probe was positioned inside the vessel. For safety reasons all experiments were conducted using pharmaceutical grade, low viscosity paraffin oil, Parafluid P130, with a viscosity of 10cSt at 40°C. It is non-flammable with a flashpoint above 150°C, non-volatile and chemically inert. Its dielectric constant was measured to 2.1 at 27°C which is similar to common nonpolar organic solvents like toluene, benzene, and cyclohexane.[33] Bulk conductivity varied due to contamination inside the experimental setup and humidity and was thus measured after each experiment. The measured values ranged from 1×10^{-13} S/m to 3×10^{-13} S/m which corresponds with relaxation times $\tau_{rel} = \epsilon/\kappa$ of 62 to 186 s. All metallic parts of the setup were individually grounded.

Oil was circulated by the pump at a constant speed to create a quasi-stationary state. During startup, the pump ran for at least 3 h until a stationary temperature of ≈35°C was reached. At this point, flow electrification in the hydraulic system had led to sufficient and approximately stationary volumetric charge densities in the liquid.

For field measurements in the gas phase the field meter was positioned above the liquid surface. A total of 172 positions with varying
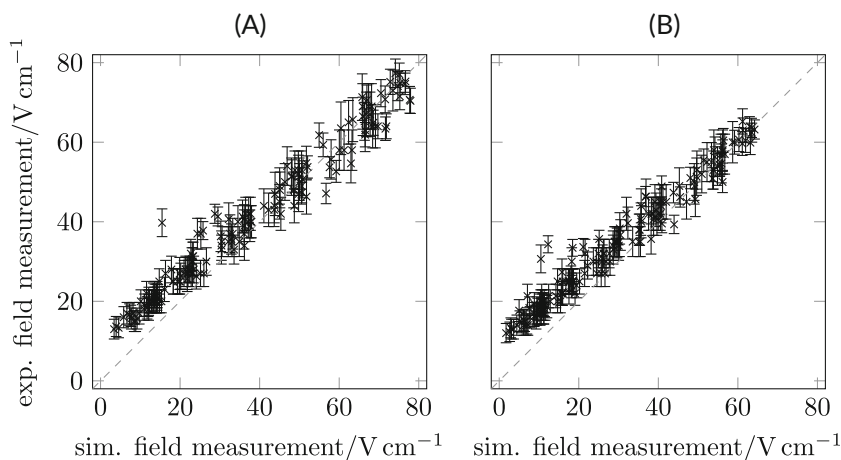
FIGURE 2 Model validation showing simulated and experimental electric field measurements for the first experiment with $\mathrm{Re} = 2351$ and $\Pi_{\mathrm{el}} = 1.081 \times 10^7$ (A) and the second with $\mathrm{Re} = 2116$ and $\Pi_{\mathrm{el}} = 1.331 \times 10^7$ (B) for all field meter positions in a scatter plot.
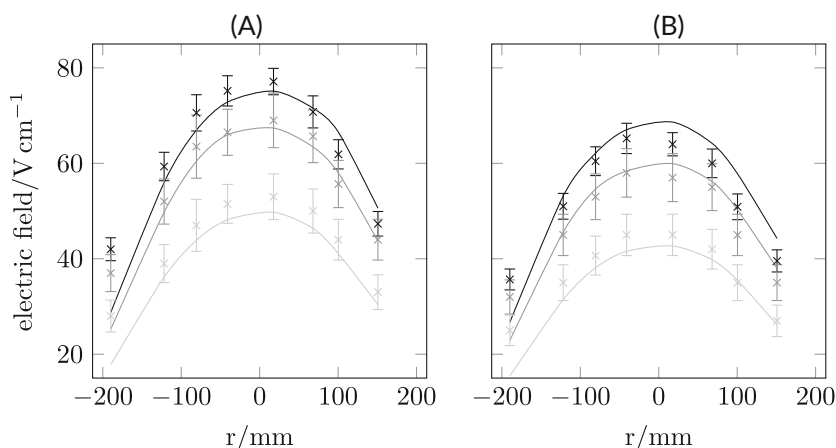

FIGURE 3 Model validation showing simulated (lines) and experimental (symbols) electric field measurements for the first experiment with $\mathrm{Re} = 2351$ and $\Pi_{\mathrm{el}} = 1.081 \times 10^7$ (A) and the second with $\mathrm{Re} = 2116$ and $\Pi_{\mathrm{el}} = 1.331 \times 10^7$ (B) along the $\alpha = 0$ axis for heights h of 36 mm (black), 46 mm (dark gray), and 76 mm (light gray).

angles α from 0° to 157.5°C, radii r from -200 to 200 mm and heights h above the liquid surface from 36 mm to 206 mm were used to measure the field throughout the gas phase. The exact positions (α, r) of the field meter, as depicted in Figure 1B, were optically measured with a camera positioned directly above the vessel and evaluated with digital image processing. The height h for each experiment was determined based on the liquid level and the geometry of the field meter rig. Positions closer to the surface than 36 mm were not used in order to minimize the risk of wetting the sensor due to waves that occurred when starting and stopping the pump. Electric field measurements at each position of the field meter were conducted three times and averaged for increased accuracy. This procedure allowed to map the electric field distribution in the gas phase above the turbulent EHD flow including errorbars.

3.2 | Influence of sensor and evaluation of volumetric charge density

The field meter is a grounded metal object and by positioning it within the gas phase above the liquid surface, it influences the electric field. Therefore, the field distribution with the field meter in place differs from the field without additional grounded objects. However, for the
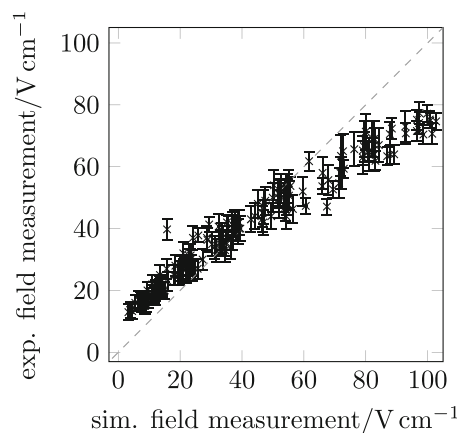

FIGURE 4 Exemplary comparison of modeling results neglecting advective transport of surface charge with experimental electric field measurements for the first experiment with $\mathrm{Re} = 2351$ and $\Pi_{\mathrm{el}} = 1.081 \times 10^7$ for all field meter positions in a scatter plot. Neglect of surface charge advection leads to systematic overestimation for field meter positions close to the surface, indicating that advective effects are essential.

experiments it was inevitable to use the field meter in different positions throughout the gas phase. For this reason, the field meter geometry was included in the simulations underlying Figures 2–4 with an

accuracy of ±0.2 mm. A field meter is based on the principle that surface charge of a conductor is proportional to the normal electric field $\sigma_s = \epsilon \mathbf{n} \cdot \mathbf{E}$. For obtaining field measurements E_m in the simulations, the integral

$$E_m = K \int_\Omega \epsilon \mathbf{n} \cdot \mathbf{E} dA, \tag{13}$$

was solved, where Ω is the area of the sensing electrode. The constant K represents the internal electronics of the field meter that translate surface charge to a measured electric field. It was calibrated inside a capacitor in separate, preliminary experiments to accurately describe the behavior of the physical field meter. During the main experiments and simulations, K was treated as a constant inherent in the used field meter. By these means, systematic errors related to the measuring procedure and equipment were accounted for during the validation. Consequently, each data point in Figures 2–4 was obtained from a separate simulation with varying field meter positions. Hereafter, the measured experimental values could be compared against the simulated measurements.

For model validation, inflowing volumetric charge density $\rho_{v,in}$ is an essential BC. As it could not be measured directly during the experiments it was extracted from the field measurements as follows. A single field measurement in the center of the vessel at $h = 106$ mm was recreated in a simulation including the position of the field meter. In the simulation, $\rho_{v,in}$ was adjusted so that the experimental and the simulated measurement obtained by Equation (13) were identical. Then, $\rho_{v,in}$ was treated as a constant parameter and set as a BC for all 171 subsequent simulations with different field meter positions. Scatter plots were used for model validation (comp. Figures 2 and 4). Inconsistencies between the model and the experiments would lead to systematic deviations between simulated and measured values for the electric field manifesting in a non-linear shape of the scatter plot. The procedure was therefore deemed suitable for model validation.

4 | RESULTS AND DISCUSSION

In this section, the presented model is validated with data from the measurements described above. Subsequently, cases with and without fluid motion are simulated and compared.

4.1 | Model validation

Two experiments were conducted for model validation. They are characterized by the two dimensionless groups

$$\mathrm{Re} = \frac{\widetilde{U}\widetilde{L}}{\nu}, \; \Pi_{el} = \frac{\rho \epsilon \widetilde{U}^2}{\widetilde{\rho}_v^2 \widetilde{L}^2},$$

with the mean inlet flow velocity $\widetilde{U}$, the diameter of the inlet pipe $\widetilde{L}$ and the volumetric charge density in the inlet $\widetilde{\rho}_v = \rho_{v,in}$. Experimental

TABLE 1 Experimental and numerical conditions for the two experiments used during model validation

Exp.	$\widetilde{U}/\mathrm{ms}^{-1}$	$\rho_{v,in}/\mathrm{cm}^{-3}$	Level/mm	Re	Π_{el}
1	0.784	9.87×10^{-7}	283	2351	1.08×10^{-7}
2	0.705	8.00×10^{-7}	257	2116	1.33×10^{-7}

Note: The liquid level is measured relative to the lower inner edge of the vessel.

and numerical conditions for the two experiments are listed in Table 1. Due to the critical Reynolds number $\mathrm{Re}_{crit} = 2040$ in pipe flow[34] and $\mathrm{Re}_{crit} = 2000$ for jet flow[35] as well as flow disturbance in the experimental setup both are considered turbulent. Higher flow rates and Reynolds numbers could not be achieved with the given experimental setup due to breakage of the silicone tubes and limited pump capacity. Figure 2A,B shows all measured values from the first (second) experiment and corresponding simulated values as a scatterplot. In case of perfect model agreement all values would be located on the diagonal. Generally, the model agrees well with the experimental values with one (two) apparent outliers at experimental values of 40 V/cm (31 V/cm and 35 V/cm). For low experimental field strengths of < 30 V/cm (< 25 V/cm) the simulated values are around 5 V/cm smaller than their experimental counterparts. This can be attributed to the fact that low measured values coincide with high values of h and thus field meter positions high above the liquid surface. As shown in Figure 1, the experimental setup was not closed and the mounting rig protruded beyond the upper edge of the vessel. Thus, the BCs in this area are not well-defined and the simulated BCs cannot replicate the experimental conditions which likely causes the apparent deviations.

In addition to global model validation, local fit was evaluated. Figure 3 shows experimental and simulated measurements along the $\alpha = 0$ axis for different heights above the liquid surface for both experiments. Most simulated values fall within the experimental error bars. Generally, measurements for the second experiment are lower due to the lower Reynolds number and thus reduced flow electrification. Overall, the model validation yields an R^2 value of 0.8918 (0.8004).

The proposed and validated model accounts for surface charge and includes advective effects. The advective term in Equation (12) dominates the behavior of surface charge as accumulation is counteracted by advection. When neglecting advection of surface charge and positioning the sensor near the liquid surface, surface charge accumulates beneath the sensor and increases the measured electric field. This effect is highlighted in Figure 4, where experimental data from the first experiment is compared with simulations neglecting advection of surface charge. Experimental measurements above 50 V/cm are systematically overestimated. The deviations increase with increasing measured fields that correspond with lower heights h above the liquid surface. Compared to Figure 2A this highlights the significance of advective effects on surface charge. Including surface charge advection thus helps unify differing results regarding the relevance of surface charge by different authors.[8–12,15–17,36]

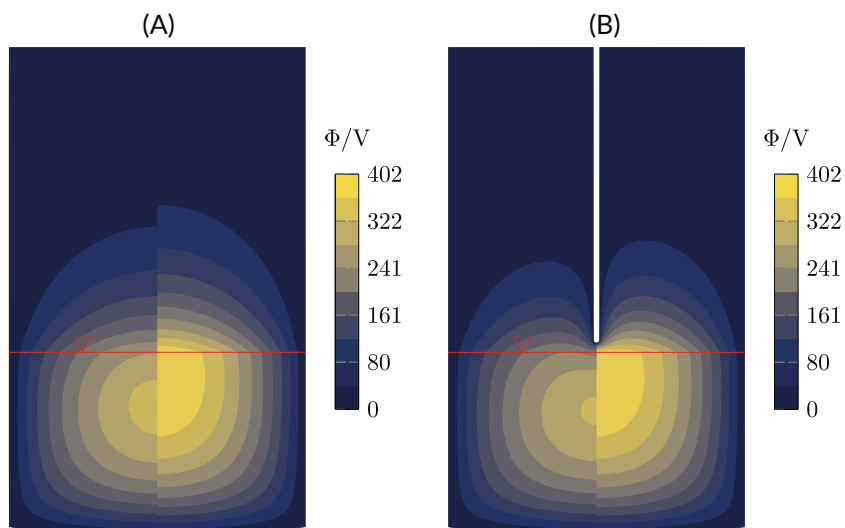(A)   (B)

FIGURE 5 Electric Potential Φ on a cross-sectional view through the middle of the vessel. The main flow direction is into the paper plane and the red line indicates the liquid surface. A flowed through vessel with $\mathrm{Re} = 2351$ and $\Pi_{\mathrm{el}} = 1.081 \times 10^7$ (split left) is compared to a vessel with liquid at rest with the same average volumetric charge density (split right), without (A) and with (B) a grounded needle above the liquid surface.
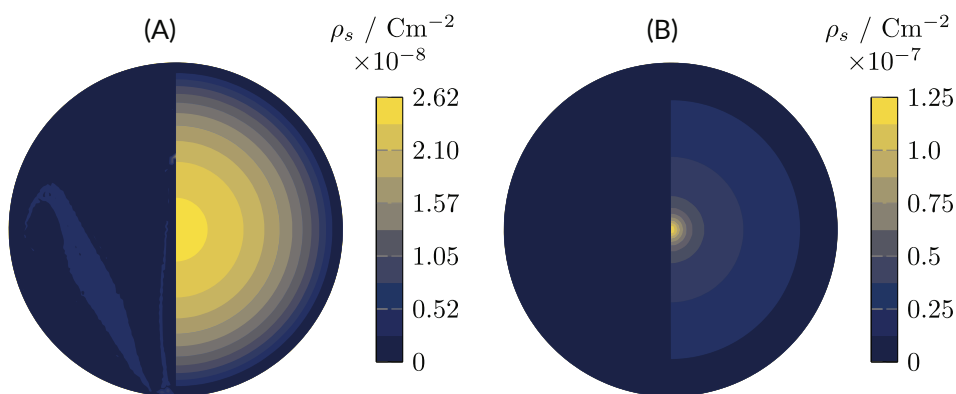
(A) $\rho_s \ / \ \mathrm{Cm}^{-2}$ (B) $\rho_s \ / \ \mathrm{Cm}^{-2}$

FIGURE 6 Surface charge density σ_s on the liquid surface of a flowed through vessel with $\mathrm{Re} = 2351$ and $\Pi_{\mathrm{el}} = 1.081 \times 10^7$ (split left) and a vessel with liquid at rest with the same average volumetric charge density (split right), without (A) and with (B) a grounded needle above the liquid surface.

Previous experiments that showed significant accumulation of surface charge were conducted at low or negligible fluid velocities while measurements at higher fluid velocities exhibited no surface charge accumulation. The model proposed in this work predicts the observable effect of diminishing accumulation of surface charge with increasing fluid velocities. To highlight this key result, the following section compares simulation results for the two scenarios of negligible fluid velocity and of turbulent jet flow.

4.2 | Influence of fluid motion on surface charge

Charged turbulent flow through a vessel with $\mathrm{Re} = 2351$ and $\Pi_{\mathrm{el}} = 1.081 \times 10^7$ is compared to the limiting case of a liquid at rest with $\mathrm{Re} = \Pi_{\mathrm{el}} = 0$. Both simulations use the same vessel geometry as in the experiments. These scenarios are representative for the two practically relevant cases of turbulent filling of a vessel and of a vessel that has been filled with charged liquid where the liquid had time to dissipate motion but not enough time for full charge relaxation. The liquid at rest in this work is assumed to carry a uniform volumetric charge density $\rho_{v,\mathrm{const}} = \rho_{v,\mathrm{in}} \exp(-\tau_{\mathrm{res}}/\tau_{\mathrm{rel}})$ with the inlet volumetric charge density $\rho_{v,\mathrm{in}}$ and residence time τ_{res} of the flowed through scenario. This ensures that the total volume charge in the

liquid is equal in both scenarios. Figure 5A shows the electric potential for both scenarios. The maximum electric field norm is $66.84\,\mathrm{V/cm}\,(69.90\,\mathrm{V/cm})$ for the flowing (resting) liquid. The maximum in electric potential is higher for the resting liquid and its position is closer to the liquid surface. This is due to the effect of accumulated surface charge, as depicted in Figure 6A. For the resting liquid, surface charge accumulates symmetrically with zero charge density at the boundaries and a maximum of $2.62 \times 10^{-8}\,\mathrm{C/m^2}$ in the middle. In case of flowing liquid the surface charge distribution resembles the streamlines of the liquid with values below $1 \times 10^{-8}\,\mathrm{C/m^2}$. The difference between the two scenarios increases when a grounded object is introduced near the liquid surface. In Figures 5B and 6B a grounded, rounded needle with a radius of 5 mm is positioned 15 mm above the surface in the center of the vessel. This is similar to the practical case of a sensor, stirrer, or filling pipe near the surface. The maximum surface charge density accumulated beneath the needle with resting liquid is one order of magnitude larger compared to the flowing liquid. This results in a higher maximum potential of 402 V compared to 326 V. The maximum electric field norm occurs at the needle surface with $955.3\,\mathrm{V/cm}\,(564.3\,\mathrm{V/cm})$ for resting (flowing) liquid. The mathematical model scales linearly with respect to ρ_v so the ratios of increased electric field and potential stay the same regardless of the absolute (inflowing) volumetric charge density.

An almost twofold increase in electric field at a grounded object for resting as opposed to flowing liquid can lead to safety hazards in practical applications. Especially, if electric fields are assessed during or shortly after filling a vessel or a tank while the liquid is still in motion, they can increase after a while and lead to electric discharges and eventually explosions.

5 | CONCLUSION

A model with reduced mathematical coupling for forced turbulent electrohydrodynamic (EHD) flows of low-conducting charged liquids has been presented. It is applicable to any Reynolds-averaged Navier–Stokes (RANS) turbulence model and predicts electric fields in the gas phase above the liquid surface in good agreement with conducted experiments. The model predicts a diminishing accumulation of surface charge at the liquid surface with increasing fluid velocities. Hereby, it unifies previous experimental and theoretical findings from literature that indicate surface charge to either be relevant or not for predicting electric fields in the gas phase. The major implication of our results for electrostatic safety in the chemical and process industry is that surface charge on the surface of a charged liquid can begin to accumulate after the liquid comes to rest. Thus, safety assessments and measurements should be conducted with low flow velocities to not underestimate electrostatic hazards. The presented model can be used in a wide variety of practical applications due to its simplicity and applicability to established RANS turbulence models. It thus provides a quantitative method for safety assessments in the chemical and process industry, where knowledge of electric fields in the gas phase above charged liquid flows is crucial for explosion prevention.

AUTHOR CONTRIBUTIONS

Aaron D. Ratschow: Conceptualization (equal); formal analysis (lead); investigation (equal); methodology (lead); software (lead); validation (lead); writing – original draft (lead). **Sigrun Stein:** Conceptualization (equal); investigation (equal); writing – review and editing (equal). **Hans-Jürgen Gross:** Funding acquisition (lead); supervision (lead); writing – review and editing (equal).

ACKNOWLEDGMENTS

DATA AVAILABILITY STATEMENT
The data that support the findings of this study are available from the corresponding author upon reasonable request.

ORCID
Aaron D. Ratschow https://orcid.org/0000-0001-6614-5008

REFERENCES

1. Cabaleiro J-M, Paillat T, Artana G, Touchard G. Flow electrification in turbulent flows of liquids—comparison of two models for one specific case. *IEEE Trans Indus Appl*. 2019;55(5):5235-5238.
2. Wagner JP, Rangel Clavijo F. Electrostatic charge generation during impeller mixing of used transformer oil. *J Electrostat*. 2000;50(1):31-47.
3. Egan S. Learning lessons from five electrostatic incidents. *J Electrostat*. 2017;88:183-189.
4. Glor M. Electrostatic ignition hazards in the process industry. *J Electrostat*. 2005;63(6–10):447-453.
5. Pratt TH, Atharton JG. Some electrostatic considerations in the transportation of flammable liquids. *Process Safety Prog*. 1996;15(3): 173-177.
6. Pratt TH, Atherton JG. Electrostatic ignitions in everyday chemical operations: three case histories. *Process Safety Prog*. 1999;18(4): 241-246.
7. Szabó SV, Kiss I, Berta I. Explosion safety in industrial electrostatics. *J Phys Conf Series*. 2011;268:012029.
8. He M, Ma Q, Zhang L. Numerical study on electrostatic potential distribution of large cylindrical oil tanks. *J Electrostat*. 2015;75:77-84.
9. Krämer H, Asano K, Schön G. Criteria for the safe filling of tank vehicles: Theoretical and experimental study to assess electrostatic hazards, 1977.
10. Wang L, Chen G, Yan D, Wang X, Liang J. Law of distribution and variation of electrostatic potential in oil tanks during filling process. *Process Safety Prog*. 2019;38(4), e12035.
11. Hunt M. Linear and nonlinear free surface flows in electrohydrodynamics. Phd thesis, 2013.
12. Kaiser MJ, Kaiser KL, Weeks WL. Surface charge representations and a finite-difference method for approximating the charge flow equation. *App Math Model*. 1994;18(4):186-197.
13. López-Herrera JM, Popinet S, Herrada MA. A charge-conservative approach for simulating electrohydrodynamic two-phase flows using volume-of-fluid. *J Comput Phys*. 2011;230(5):1939-1955.
14. Songoro H. *Electrohydrodynamic Modeling of Droplet Vibrations under the Influence of Electric Fields*. PhD thesis. Technische Universität; 2015.
15. Walmsley HL. Voltage calculations for annular tanks partly-filled with charged liquid. *J Electrostat*. 2013;71(6):1011-1019.
16. Krämer H, Asano K. Incendivity of sparks from surfaces of electrostatically charged liquids. *J Electrostat*. 1979;6(4):361-371.
17. Matsubara Y, Jones TB. Numerical modeling for potential relaxation of charged oil in containers. *IEEE Trans Indus Appl*. 1993;29(2): 295-299.
18. Matsubara Y. Measurement of surface conductivity in dielectric liquid. *J Electrostat*. 1999;46(2–3):125-130.
19. Hanjalić K, Launder BE. Eddy-viscosity transport modelling: a historical review. In: Runchal A, ed. *50 Years of CFD in Engineering Sciences*. Vol 23. Springer; 2020:295-316.
20. Probstein RF. *Physicochemical Hydrodynamics*. John Wiley & Sons, Inc; 1994.
21. Zhakin AI. Electrohydrodynamics. *Physics-Uspekhi*. 2012;55(5):465-488.
22. Abedian B, Sonin AA. Theory for electric charging in turbulent pipe flow. *J Fluid Mech*. 1982;120:199-217.
23. Zmarzly D. Streaming electrification current model in a round pipe in turbulent regime. *IEEE Trans Dielectric Electric Insulat*. 2013;20(5): 1497-1509.
24. Baldyga J, Bourne JR. *Turbulent Mixing and Chemical Reactions*. Wiley; 1999.
25. Gualtieri C, Angeloudis A, Bombardelli F, Jha S, Stoesser T. On the values for the turbulent schmidt number in environmental flows. *Fluids*. 2017;2(2):17.
26. Kays WM, Crawford ME. *Convective Heat and Mass Transfer. McGraw-Hill Series in Mechanical Engineering*. 3rd. ed. McGraw-Hill; 1993.

27. Kallendorf C, Cheviakov AF, Oberlack M, Wang Y. Conservation laws of surfactant transport equations. *Phys Fluids*. 2012;24(10):102105.

28. Comsol Inc. Cfd module user's guide, version 5.5: Fully developed flow (inlet). 159–160, 2019.

29. Comsol Inc. Comsol multiphysics version 5.5.

30. Wilcox DC. *Turbulence Modeling for CFD*. DCW Industries; 1994.

31. Cebeci T. *Analysis of Turbulent Flows with Computer Programs*. 3rd ed. Elsevier Science; 2013.

32. Comsol Inc. Comsol mulitphysics reference manual, version 5.5: The adaptive mesh refinement solver. 1302–1304, 2019.

33. Myers BJ. Common Solvents Used in Organic Chemistry: Table of Properties. 2020.

34. Avila K, Moxey D, de Lozar A, Avila M, Barkley D, Hof B. The onset of turbulence in pipe flow. *Science (New York, N.Y.)*. 2011;333(6039): 192-196.

35. Lee JHW, Chu VH. Turbulent jets. In: Lee JHW, Chu VH, eds. *Turbulent Jets and Plumes*. Springer; 2003:21-54.

36. Matsubara Y, Jones TB. Observation of transient charge relaxation of oil within a cylindrical vessel. In Conference Record of the 1993 IEEE Industry Applications Conference Twenty-Eighth IAS Annual Meeting. 1704–1708. IEEE, 1993.

APPENDIX A: Model expansion for free surface and two-phase flows

The model presented in the main text approximates the free surface of the liquid as a fixed boundary with zero tangential stress. This simplification is valid when free surface deformation is negligible, like in the conducted experiments. However, more general industrial flow applications may exhibit significant free surface deformations. The more general model presented in this appendix takes this into account. While the modeled problems include a liquid and a gas phase, the viscosity and density of the gas phase, most commonly air, are often very small compared to the liquid phase. Thus, viscous stresses of the air at the free surface are negligible and the flow field must only be solved in the liquid phase. The liquid flow is governed by the incompressible RANS equations,

$$\frac{\partial \mathbf{u}}{\partial t} + (\mathbf{u} \cdot \nabla)\mathbf{u} = -\frac{1}{\rho}\nabla p$$
$$+ \nabla \cdot (\nu + \nu_T)\left[\nabla \mathbf{u} + (\nabla \mathbf{u})^T\right] + \frac{1}{\rho}(\mathbf{f}_{el} + \mathbf{f}_g), \tag{A1}$$

$$\nabla \cdot \mathbf{u} = 0, \tag{A2}$$

where in this case Boussinesq's eddy viscosity hypothesis is already incorporated. Here, $\mathbf{f}_g$ denotes the gravitational force and $\mathbf{f}_{el}$ the Lorentz force which can be neglected in the case of $\Pi_{el} > \mathrm{Re} \gg 1$. An appropriate eddy viscosity model is required for closure. Additionally, balance Equations (10) and (12) for ρ_v and σ_s are solved in the liquid phase and on the interface respectively and the Poisson Equation (1b) is solved in both the liquid and gas phases. These governing equations are coupled by interfacial conditions. The electric field is not continuous through the interface in the presence of surface charge but obeys $\mathbf{n} \cdot [\![\epsilon \mathbf{E}]\!] = \sigma_s$. Since viscous stresses of the air are neglected and assuming a constant surface tension γ, tangential stresses originate exclusively from interfacial charge σ_s. The tangential stress balance at the interface becomes

$$\mathbf{t} \cdot \tau \cdot \mathbf{n} + \sigma_s \mathbf{E}_l \cdot \mathbf{t} = 0, \tag{A3}$$

where $\mathbf{t}$ is any tangential vector and $\tau = \rho(\nu + \nu_T)\left[\nabla \mathbf{u} + (\nabla \mathbf{u})^T\right]$ is the viscous stress tensor. Indices l and g denote the liquid and gas phase respectively. The normal stress balance at the interface,

$$(p_l - p_g) - \mathbf{n} \cdot \tau \cdot \mathbf{n} + \frac{1}{2}\sigma_s(\mathbf{E}_l + \mathbf{E}_g) \cdot \mathbf{n} - \frac{1}{2}(\epsilon_l - \epsilon_g)(\mathbf{E}_l \cdot \mathbf{E}_g)$$
$$= \gamma(\nabla_s \cdot \mathbf{n}), \tag{A4}$$

accounts for a pressure jump due to surface tension and electric forces.[14] Ultimately, the interface must obey the kinematic condition

$$\mathbf{u}_s = \mathbf{u}, \tag{A5}$$

where $\mathbf{u}_s$ is the velocity of the interface. The numerical method of tracking the interface depends on the code used to solve the equations. This model can also be expanded to two-phase flow configurations by considering interfacial tension forces in Equation (A1) and replacing τ with $[\![\tau]\!]$ in Equations (A3) and (A4).